CFSRC COLLOQUIUM

Proceedings of the Cold-Formed Steel Research Consortium Colloquium
20-22 October, 2020 (cfsrc.org)

Linear and bifurcation analyses combining shell and GBT-based beam finite elements

David Manta[1], Rodrigo Gonçalves[2], Dinar Camotim[3]

Abstract

This paper concerns a general and very efficient approach to model thin-walled members with complex geometries (including taper and/or connected through joints), which combines standard shell and GBT-based finite elements. This approach (i) allows a straightforward modelling of complex geometries and (ii) is very efficient from a computational point of view, as the shell model substructures can be condensed out of the global equilibrium equations. The capabilities of the proposed approach are demonstrated through several examples concerning the linear and bifurcation (linear stability) analyses of (i) members with tapered segments, (ii) members with holes and (iii) beam-column assemblies. The results obtained are compared with full shell finite element model solutions and an excellent match is obtained.

1. Introduction

Generalised Beam Theory (GBT) is nowadays well-established as an efficient tool to analyse thin-walled bars subjected to global/distortional/local deformation. Its main advantages arise from the modal decomposition of the beam kinematics in a set of so-called "cross-section deformation modes", which constitute a distinct feature of GBT and lead to accurate solutions even when just a few of them are used in the analysis. This leads to major computational gains, which are particularly evident in the context of linear and bifurcation (linear stability) analyses.

Since the pioneer works of Schardt [1], [2] (see http://vtb.info for a complete list of publications of the Darmstad-based group), GBT has been considerably developed by several researchers, most notably the Lisbon-based research group (see, e.g. [3], [4] and http://www.civil.ist.utl.pt/gbt for an updated list of publications). GBT constitutes an extension of the Vlasov prismatic bar theory and therefore its application to non-prismatic members is not straightforward. In this respect the following research efforts are worth mentioning. Moderately tapered members are treated in [5] and conical shells in [6], [7]. Members with holes have been addressed in [8], although at the expense of requiring a refined cross-section discretisation (and only the membrane longitudinal normal pre-buckling stresses are taken into account). A general approach for members with holes, discrete thickness variation, plasticity and geometrical non-linearity was proposed in [9], using non-orthogonal deformation modes to improve the computational efficiency (the orthogonal modes are retrieved through post-processing the results). A linear formulation for members with circular axis was proposed in [10], [11]. Finally, frames have been dealt with using carefully chosen constraints between connecting members [12]–[15].

This paper proposes an alternative and more general approach, where shell and GBT-based (beam) finite elements are combined to allow handling, rather straightforwardly, complex geometries. In essence, the GBT elements are used to model prismatic members, while shell elements are adopted in the remaining zones (tapering, holes, joints, etc.). This subdivision makes it possible to include only a small number of deformation modes in the GBT elements without sacrificing accuracy, since the zones with concentrated stresses/strains, usually requiring many deformation modes to be correctly modelled with GBT, are handled by the shell elements. Although this paper addresses linear (first-order) and bifurcation (linear stability) analyses, since the GBT approach is most effective in this context, the procedure is currently being extended by the authors to cover other analysis types.

The outline of the paper is as follows. Section 2 presents the fundamentals of the adopted GBT-based and shell finite elements. Section 3, discusses the procedure adopted for com-

[1]CERIS and Departamento de Engenharia Civil, Faculdade de Ciências e Tecnologia, Universidade Nova de Lisboa, 2829-516, Caparica, Portugal, d.manta@campus.fct.unl.pt

[2]CERIS and Departamento de Engenharia Civil, Faculdade de Ciências e Tecnologia, Universidade Nova de Lisboa, 2829-516, Caparica, Portugal, rodrigo.goncalves@fct.unl.pt

[3]CERIS, ICIST, DECivil, Instituto Superior Técnico, Universidade de Lisboa, Av. Rovisco Pais, 1049-001 Lisboa, Portugal, dcamotim@civil.ist.utl.pt

bining GBT and shell elements. Next, Section 4 presents three numerical examples that demonstrate the capabilities of the proposed approach. For comparison purposes, solutions obtained with full shell finite element models are provided. Finally, the paper closes in Section 5, with the concluding remarks.

2. The adopted shell and GBT-based finite elements

This section presents the fundamentals of the selected shell and GBT-based finite elements, as well as their combination. Concerning the notation, scalars are represented in *italic* letters and vectors/matrices in **bold** letters. The usual identity matrix is displayed as $\mathbf{1}$ and matrices/vectors with null entries as $\mathbf{0}$. The standard Euclidean inner product between two vectors of arbitrary dimension $\boldsymbol{a}$ and $\boldsymbol{b}$ is written as $\boldsymbol{a} \cdot \boldsymbol{b}$, a derivative is represented by a subscript comma (e.g. $f_{,a} = \partial f / \partial a$), a virtual variation is denoted by δ and an incremental variation by Δ. Moreover, h is the shell/wall thickness.

In the present work, Green-Lagrange strains $\boldsymbol{E}$ are adopted, together with their work-conjugate second Piola-Kirchhoff stresses $\boldsymbol{S}$. Therefore, using a Voigt-like notation, the equilibrium equations are obtained from the virtual work statement

$$\delta W = -\int_V \delta \boldsymbol{E} \cdot \boldsymbol{S} \, \mathrm{d}V + \int_\Omega \delta \bar{\boldsymbol{U}} \cdot \boldsymbol{q} \, \mathrm{d}\Omega = 0, \tag{1}$$

where V and Ω are the thin-walled member volume and mid-surface, respectively, at the initial configuration, and it is assumed that the external loads, $\boldsymbol{q}$, are applied at the element mid-surface only, where $\bar{\boldsymbol{U}}$ are the work-conjugate mid-surface displacements.

In addition, a linear elastic stress-strain relation is assumed, of the form

$$\boldsymbol{S} = \boldsymbol{C}\boldsymbol{E}, \tag{2}$$

where $\boldsymbol{C}$ is the constitutive matrix. A St. Venant-Kirchhoff material law is adopted, written in terms of Young's modulus E, the shear modulus G and Poisson's ratio ν.

Next, a distinction is made between two cases. Firstly, the linear analysis case, where Green-Lagrange strains become small strains $\boldsymbol{\varepsilon}$ and the internal virtual work is given by

$$\delta W_{int} = -\int_V \delta \boldsymbol{\varepsilon} \cdot \boldsymbol{C}\boldsymbol{\varepsilon} \, \mathrm{d}V. \tag{3}$$

Secondly, the linear stability analysis case is considered. A preliminary linear pre-buckling analysis must be performed to retrieve the pre-buckling stresses. Recalling that thin-walled members are being addressed, both the shell and GBT formulations used in this work only retain the membrane part of these stresses, $\bar{\boldsymbol{S}}$. Therefore, the linearisation of Equation (1) at the initial configuration leads to the bifurcation equation

$$\Delta\delta W_{int}(\boldsymbol{\phi} = \mathbf{0}, \lambda) = -\int_V \left(\delta \boldsymbol{\varepsilon} \cdot \boldsymbol{C} \Delta \boldsymbol{\varepsilon} + \Delta \delta \boldsymbol{E} \cdot \lambda \bar{\boldsymbol{S}} \right) \mathrm{d}V, \tag{4}$$

where $\boldsymbol{\phi}$ is a vector that collects the kinematic variables (with $\boldsymbol{\phi} = \mathbf{0}$ referring to the initial configuration) and λ is the load multiplier, which is assumed to be directly proportional to the stresses $\bar{\boldsymbol{S}}$ (calculated for $\lambda = 1$). The first and second terms in Equation (4) lead to the finite element linear and geometric stiffness matrices, respectively.

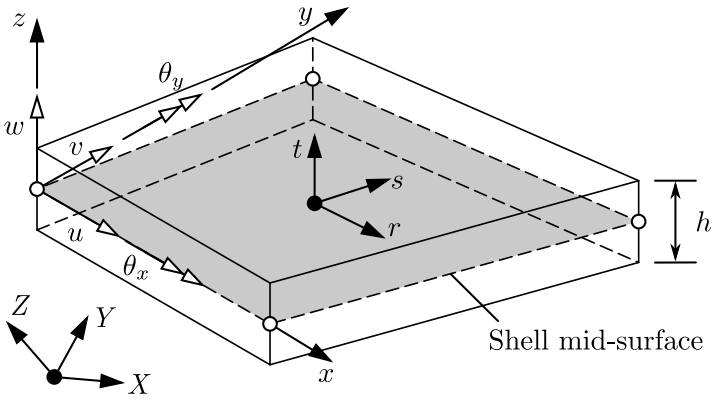

Figure 1: MITC-4 reference systems and displacement components.

2.1 The MITC-4 shell finite element

In this work, a 4-node shell finite element with a Reissner-Mindlin kinematic description is adopted. It is well known that, in this case, a pure displacement-based interpolation will lead to shear locking. This phenomenon is circumvented using the Mixed Interpolation of Tensorial Component (MITC) strategy developed by Bathe and co-workers (see, e.g., [16], [17]). According to Figure 1, three reference systems are defined: (i) the global Cartesian system (X, Y, Z), (ii) the element Cartesian local axes (x, y, z), where x is attached to one of the element lateral faces, and (iii) a convected frame (r, s, t), where t is assumed coincident with the local z axis, defining the through-thickness direction (the shell is initially flat).

Following the Reissner-Mindlin hypothesis, the mid-surface displacements u, v, w and the rotations θ_x, θ_y along the local axes (see Figure 1) constitute the necessary and sufficient kinematic variables to completely describe the element displacement field $\boldsymbol{U}$, through

$$\boldsymbol{U}(x,y,z) = \begin{bmatrix} U_x \\ U_y \\ U_z \end{bmatrix} = \begin{bmatrix} u(x,y) + z\theta_y(x,y) \\ v(x,y) - z\theta_x(x,y) \\ w(x,y) \end{bmatrix}. \tag{5}$$

In the local Cartesian system, adopting Voigt-like vector forms, the Green-Lagrange strains are subdivided into membrane (M), bending (B) and shear (S) components, and only

the non-linear part of the membrane components is retained, reading

$$\boldsymbol{E}^M = \begin{bmatrix} E^M_{xx} \\ E^M_{yy} \\ 2E^M_{xy} \end{bmatrix} = \begin{bmatrix} u_{,x} \\ v_{,y} \\ u_{,y} + v_{,x} \end{bmatrix} + \frac{1}{2} \begin{bmatrix} \bar{\boldsymbol{U}}_{,x} \cdot \bar{\boldsymbol{U}}_{,x} \\ \bar{\boldsymbol{U}}_{,y} \cdot \bar{\boldsymbol{U}}_{,y} \\ 2\bar{\boldsymbol{U}}_{,x} \cdot \bar{\boldsymbol{U}}_{,y} \end{bmatrix}, \quad (6)$$

$$\boldsymbol{E}^B = \begin{bmatrix} E^B_{xx} \\ E^B_{yy} \\ 2E^B_{xy} \end{bmatrix} = z \begin{bmatrix} \theta_{y,x} \\ -\theta_{x,y} \\ \theta_{y,y} - \theta_{x,x} \end{bmatrix}, \quad (7)$$

$$\boldsymbol{E}^S = \begin{bmatrix} 2E_{xz} \\ 2E_{yz} \end{bmatrix} = \begin{bmatrix} w_{,x} + \theta_y \\ w_{,y} - \theta_x \end{bmatrix}, \quad (8)$$

with $\bar{\boldsymbol{U}}^T = [u \;\; v \;\; w]$ being the mid-surface displacement vector. Although membrane locking is not present in the context of linear and bifurcation analyses (the element is initially flat), shear locking may occur and is mitigated with the MITC approach by re-interpolating the covariant through-thickness shear strains from their values at the so-called "tying points" (see [17], [18] for details).

Concerning the stresses, a plane stress state is assumed ($S_{zz} = 0$), leading to

$$\boldsymbol{S}^M = \bar{\boldsymbol{C}}\boldsymbol{E}^M, \quad \boldsymbol{S}^B = \bar{\boldsymbol{C}}\boldsymbol{E}^B, \quad \boldsymbol{S}^S = G\boldsymbol{E}^S, \quad (9)$$

$$\bar{\boldsymbol{C}} = \frac{E}{1-\nu^2} \begin{bmatrix} 1 & \nu & 0 \\ \nu & 1 & 0 \\ 0 & 0 & \frac{1-\nu}{2} \end{bmatrix}. \quad (10)$$

The finite element equations are obtained by interpolating the mid-surface displacements and rotations using linear functions and following a standard isoparametric approach. The independent kinematic variables are collected in the vector

$$\boldsymbol{\phi}^T = \begin{bmatrix} u & v & w & \theta_x & \theta_y \end{bmatrix}, \quad (11)$$

and the interpolation is then given by $\boldsymbol{\phi} = \boldsymbol{\Psi}\boldsymbol{d}$, where $\boldsymbol{\Psi}$ is a matrix containing the interpolation functions

$$\boldsymbol{\Psi}^T = \begin{bmatrix} \boldsymbol{\psi}^T_u & \boldsymbol{\psi}^T_v & \boldsymbol{\psi}^T_w & \boldsymbol{\psi}^T_{\theta_x} & \boldsymbol{\psi}^T_{\theta_y} \end{bmatrix}, \quad (12)$$

where $\boldsymbol{\psi}_{(\cdot)}$ are the suitable sub-matrices that match the components of the vector of nodal unknowns

$$\boldsymbol{d}^T = \begin{bmatrix} u_1 & v_1 & w_1 & (\theta_x)_1 & (\theta_y)_1 & \dots \\ & & & & & \dots \;\; u_4 \;\; v_4 \;\; w_4 \;\; (\theta_x)_4 \;\; (\theta_y)_4 \end{bmatrix}. \quad (13)$$

For a linear analysis, recalling Equation (3), the element stiffness matrix is given by

$$\boldsymbol{K}_e = \int_V \left(\boldsymbol{B}^T_M \bar{\boldsymbol{C}} \boldsymbol{B}_M + \boldsymbol{B}^T_B \bar{\boldsymbol{C}} \boldsymbol{B}_B + G \boldsymbol{B}^T_S \boldsymbol{B}_S \right) \mathrm{d}V, \quad (14)$$

were the full expressions of the strain-displacement matrices $\boldsymbol{B}_M$, $\boldsymbol{B}_B$ are given in [18] and $\boldsymbol{B}_S$ can be found in [16].

Lastly, for the linear stability analyses, from the final term of Equation (4), the element geometric matrix is obtained as

$$\boldsymbol{G}_e = \lambda \int_V \Big(\bar{S}^M_{xx} \bar{\boldsymbol{B}}^T_{xx} \bar{\boldsymbol{B}}_{xx} + \bar{S}^M_{yy} \bar{\boldsymbol{B}}^T_{yy} \bar{\boldsymbol{B}}_{yy} + \\ + \bar{S}^M_{xy} \left(\bar{\boldsymbol{B}}^T_{xx} \bar{\boldsymbol{B}}_{yy} + \bar{\boldsymbol{B}}^T_{yy} \bar{\boldsymbol{B}}_{xx} \right) \Big) \mathrm{d}V, \quad (15)$$

with the auxiliary matrices $\bar{\boldsymbol{B}}_{xx}$ and $\bar{\boldsymbol{B}}_{yy}$ being provided in [18].

For the computation of these matrices, numerical integration is performed using a 2×2 Gauss point grid along the shell mid-surface. Along the thickness direction, since only elastic examples are addressed in this paper, analytical integration is performed.

2.2 The GBT-based finite element

The GBT element employed in this work follows that proposed in [19], although some simplifications are introduced, namely: (i) geometrical imperfections are disregarded, (ii) simplifications are introduced to the membrane stress and strain fields, (iii) a linear elastic material is assumed and (iv) in the context of a linear stability analysis, only the non-linear strain terms associated with the membrane longitudinal extensions are considered, which is acceptable for slender bars.

Figure 2 depicts (i) an arbitrary prismatic thin-walled bar, composed by two walls, (ii) the global Cartesian axes (X, Y, Z), where X defines the member longitudinal axis, and (iii) the local Cartesian axes for each wall (x, y, z), defining the member axis, wall mid-line and thickness directions, respectively. In accordance with the classic GBT approach, Kirchhoff's thin plate assumption is adopted and the displacement vector for each wall is expressed, in the local axes, as

$$\boldsymbol{U}(x,y,z) = \begin{bmatrix} U_x \\ U_y \\ U_z \end{bmatrix} = \begin{bmatrix} (\bar{\boldsymbol{u}} - z\bar{\boldsymbol{w}}) \cdot \boldsymbol{\phi}_{,x} \\ (\bar{\boldsymbol{v}} - z\bar{\boldsymbol{w}}_{,y}) \cdot \boldsymbol{\phi} \\ \bar{\boldsymbol{w}} \cdot \boldsymbol{\phi} \end{bmatrix}, \quad (16)$$

where $\bar{\boldsymbol{u}}(y)$, $\bar{\boldsymbol{v}}(y)$, $\bar{\boldsymbol{w}}(y)$ are column vectors containing the deformation mode displacement components along x, y and z, respectively, and $\boldsymbol{\phi}(x)$ is a column vector collecting the amplitude functions of each deformation mode (the problem unknowns). The deformation modes are a function of the cross-section geometry and material parameters, and their displacement components are obtained from the so-called "GBT cross-section analysis", explained in detail in [20], [21] and implemented in the GBTUL program [22], available for download as freeware at www.civil.ist.utl.pt/gbt. Essentially, the GBT cross-section analysis begins with the cross-section discretisation into mandatory "natural" nodes, located at wall mid-line intersections and free ends, and "intermediate nodes", arbitrarily located in each wall mid-line.

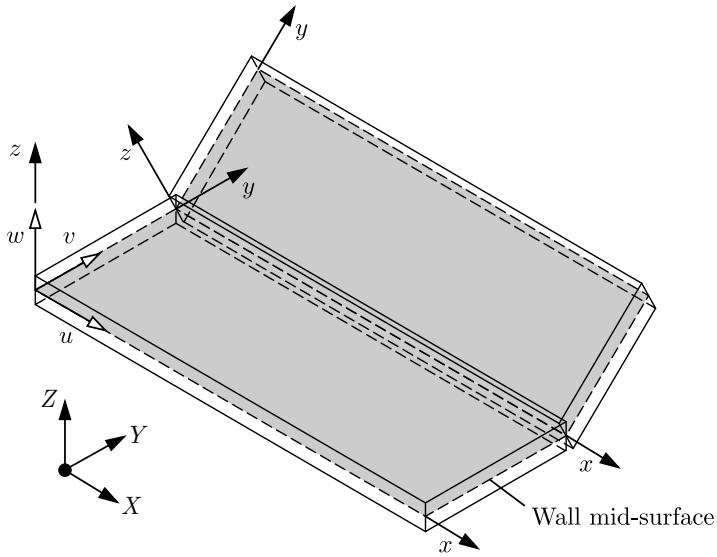

Figure 2: Arbitrary thin-walled member geometry, global/local coordinate systems and local displacement components.

The in-plane/warping displacements of these nodes constitute the basis for the definition of the cross-section deformation modes. Subsequently, an appropriate change of basis is performed to obtain a hierarchical and structurally meaningful set of deformation modes.

In a linear analysis context, the non-null small strain components (for each wall) are stored in vector $\boldsymbol{\varepsilon}$, reading

$$\boldsymbol{\varepsilon} = \begin{bmatrix} \varepsilon_{xx} \\ \varepsilon_{yy} \\ \gamma_{xy} \end{bmatrix} = \begin{bmatrix} (\bar{\boldsymbol{u}} - z\bar{\boldsymbol{w}}) \cdot \boldsymbol{\phi}_{,xx} \\ (\bar{\boldsymbol{v}}_{,y} - z\bar{\boldsymbol{w}}_{,yy}) \cdot \boldsymbol{\phi} \\ (\bar{\boldsymbol{u}}_{,y} + \bar{\boldsymbol{v}} - 2z\bar{\boldsymbol{w}}_{,y}) \cdot \boldsymbol{\phi}_{,x} \end{bmatrix}, \tag{17}$$

where the membrane/bending terms are constant/linear along the thickness direction z, respectively.

With the purpose of reducing the deformation modes included in the analyses, without compromising accuracy, in beam-type problems two constraints are usually adopted: (i) null membrane transverse strains ($\varepsilon_{yy}^M = 0$) and (ii) null membrane shear strains ($\gamma_{xy}^M = 0$, the so-called Vlasov's assumption). These two assumptions are always employed in this paper, recalling that the contribution of this work consists of modelling (i) complex zones with shell elements and (ii) the remaining (prismatic) zones with GBT elements including just a few deformation modes. With the above strain constraints, only two deformation mode sets are obtained: (i) natural Vlasov modes (axial extension, bending, torsion and several distortional modes) and (ii) local-plate modes.

For the calculation of bifurcation loads, only the Green-Lagrange longitudinal membrane strains are required, as already mentioned. The relevant Green-Lagrange strains are therefore grouped in vector $\boldsymbol{E}^T = [E_{xx}\ \varepsilon_{yy}\ \gamma_{xy}]^T$, with

$$E_{xx}^M = \varepsilon_{xx} + \frac{1}{2}\left(\boldsymbol{\phi}_{,x}^T\left(\bar{\boldsymbol{v}}\bar{\boldsymbol{v}}^T + \bar{\boldsymbol{w}}\bar{\boldsymbol{w}}^T\right)\boldsymbol{\phi}_{,x} + \boldsymbol{\phi}_{,xx}^T\bar{\boldsymbol{u}}\bar{\boldsymbol{u}}^T\boldsymbol{\phi}_{,xx}\right). \tag{18}$$

In addition, the term $\bar{\boldsymbol{u}}\bar{\boldsymbol{u}}^T$ may be discarded without significant loss of accuracy [23].

For the stresses, a plane stress state is assumed, with $\boldsymbol{S}^T = [S_{xx}\ S_{yy}\ S_{xy}]$. However, due to the null transverse membrane strain constraint, the membrane and bending stresses are separated in order to avoid over-stiff solutions, leading to

$$\boldsymbol{S}^M = \boldsymbol{C}^M\boldsymbol{E}^M, \quad \boldsymbol{S}^B = \bar{\boldsymbol{C}}\boldsymbol{E}^B, \tag{19}$$

$$\boldsymbol{C}^M = \begin{bmatrix} E & 0 & 0 \\ 0 & 0 & 0 \\ 0 & 0 & 0 \end{bmatrix}. \tag{20}$$

The finite element is obtained by interpolating the amplitude functions by means of Hermite cubic polynomials for all deformation modes except those involving only warping (e.g., the axial extension mode), in which case quadratic Lagrange functions are employed. As in the case of the shell elements, the interpolation is of the form $\boldsymbol{\phi} = \boldsymbol{\Psi}\boldsymbol{d}$, where matrix $\boldsymbol{\Psi}$ contains the interpolation functions and $\boldsymbol{d}$ is the vector of unknowns.

For a linear analysis, from (3), the element stiffness matrix reads

$$\boldsymbol{K}_e = \int_L \begin{bmatrix} \boldsymbol{\Psi} \\ \boldsymbol{\Psi}_{,x} \\ \boldsymbol{\Psi}_{,xx} \end{bmatrix}^T \begin{bmatrix} \mathbf{B} & \mathbf{0} & \mathbf{D}_2 \\ \mathbf{0} & \mathbf{D}_1 & \mathbf{0} \\ \mathbf{D}_2^T & \mathbf{0} & \mathbf{C} \end{bmatrix} \begin{bmatrix} \boldsymbol{\Psi} \\ \boldsymbol{\Psi}_{,x} \\ \boldsymbol{\Psi}_{,xx} \end{bmatrix} \mathrm{d}x, \tag{21}$$

where L is the member initial length and the GBT modal matrices are given by

$$\mathbf{B} = \int_S \frac{Eh^3}{12(1-\nu^2)}\bar{\boldsymbol{w}}_{,yy}\bar{\boldsymbol{w}}_{,yy}^T\,\mathrm{d}y, \tag{22}$$

$$\mathbf{C} = \int_S \left(Eh\bar{\boldsymbol{u}}\bar{\boldsymbol{u}}^T + \frac{Eh^3}{12(1-\nu^2)}\bar{\boldsymbol{w}}\bar{\boldsymbol{w}}^T\right)\mathrm{d}y, \tag{23}$$

$$\mathbf{D}_1 = \int_S \frac{Gh^3}{3}\bar{\boldsymbol{w}}_{,y}\bar{\boldsymbol{w}}_{,y}^T\,\mathrm{d}y, \tag{24}$$

$$\mathbf{D}_2 = \int_S \frac{\nu Eh^3}{12(1-\nu^2)}\bar{\boldsymbol{w}}_{,yy}\bar{\boldsymbol{w}}^T\,\mathrm{d}y, \tag{25}$$

where S is the cross-section mid-line. It is worth-noting that membrane/bending terms are multiplied by h/h^3, respectively.

Finally, for linear stability analyses, from Equation (4), the element geometric matrix reads

$$\boldsymbol{G}_e = \lambda\int_L\int_S h\bar{S}_{xx}^M\boldsymbol{\Psi}_{,x}^T(\bar{\boldsymbol{v}}\bar{\boldsymbol{v}}^T + \bar{\boldsymbol{w}}\bar{\boldsymbol{w}}^T)\boldsymbol{\Psi}_{,x}\mathrm{d}y\,\mathrm{d}x. \tag{26}$$

3. Combining shell and GBT-based finite elements

As previously mentioned, the focus of the proposed approach is to combine the versatility of shell elements to model zones (shell substructures or macro-elements) where a complex behaviour is expected, with the computational efficiency of the GBT-based elements to model the regular/smooth zones, where just a few deformation modes are required to capture the beam displacement field.

As an illustrative example, Figure 3 depicts an assembly of two GBT-based (beam) finite elements and a shell macro-element, concerning a single beam wall. The connection detail shows (i) "linked nodes" (nodes shared by the shell and GBT models) and also (ii) "hanging nodes" (see, e.g., [24]), which appear due to the fact that the cross-section discretisation is generally coarser in the GBT model. In general, the constraint equations should apply to both types of nodes, to ensure compatibility. However, if the shell macro-element zone is extended so that severe localized deformation does not occur at the GBT-shell interface, the constraints for the hanging nodes can be discarded without significant loss of accuracy. This approach is followed in this work, being further discussed in Section 4.

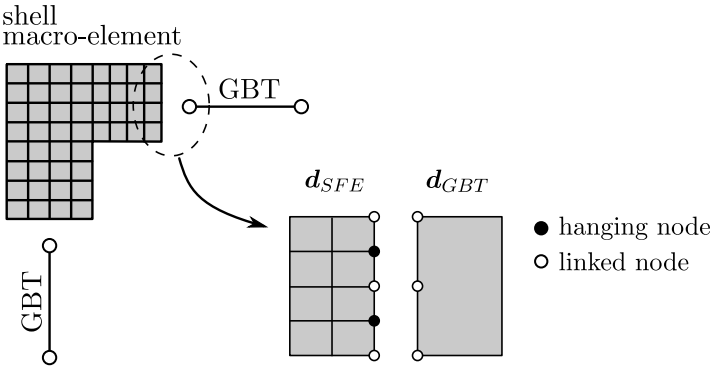

Figure 3: Coupling between a shell macro-element and two GBT finite elements.

At a boundary connecting shell and GBT elements, compatibility is enforced through constraint equations of the form

$$\zeta_j \left(U_{kj}^{SFE}(z=0) - U_{kj}^{GBT}(z=0) \right) = 0, \tag{27}$$

where ζ_j are Lagrange multipliers and U_{kj}^{GBT}, U_{kj}^{SFE} are the displacements of the mid-surface $(z=0)$ node k along direction j, in the GBT and shell discretisations, respectively. Since only the mid-surface nodal displacements are constrained (i.e., the shell nodal rotation DOFs are not constrained), this procedure leads to a loss of compatibility across the shell/GBT interface. However, this issue has little relevance for thin-walled members, where through-thickness shearing is generally negligible. If this effect is important, it must be minimized by extending the shell macro-element zone — this issue will be addressed in the numerical examples presented in Section 4.

The constraint equations can be cast as

$$\boldsymbol{\zeta}^T \left(\boldsymbol{B}_{SFE}\, \boldsymbol{d}_{SFE} - \boldsymbol{B}_{GBT}\, \boldsymbol{d}_{GBT} \right) = 0, \tag{28}$$

where $\boldsymbol{\zeta}$ is a column vector collecting all the Lagrange multipliers, $\boldsymbol{d}_{SFE}$ and $\boldsymbol{d}_{GBT}$ are the components of vector $\boldsymbol{d}$ of the shell and GBT finite elements, respectively, and the auxiliary matrices $\boldsymbol{B}_{SFE}$ and $\boldsymbol{B}_{GBT}$ contain the coefficients of the constraint equations.

Matrix $\boldsymbol{B}_{SFE}$ can be obtained by introducing a single unit entry at each row, corresponding to the selected shell displacement to constrain. For the computation of matrix $\boldsymbol{B}_{GBT}$, the deformation modes are first calculated using GBTUL and then Equation (16) is employed to calculate the corresponding displacement, with $z=0$ (mid-line) and $\boldsymbol{\phi} = \boldsymbol{\Psi}\boldsymbol{d}_{GBT}$. Naturally, if the axes do not match, a coordinate transformation is necessary.

The resulting equation system reads

$$\begin{bmatrix} \boldsymbol{K}_{SFE} & \boldsymbol{0} & \boldsymbol{B}_{SFE}^T \\ \boldsymbol{0} & \boldsymbol{K}_{GBT} & -\boldsymbol{B}_{GBT}^T \\ \boldsymbol{B}_{SFE} & -\boldsymbol{B}_{GBT} & \boldsymbol{0} \end{bmatrix} \begin{bmatrix} \boldsymbol{d}_{SFE} \\ \boldsymbol{d}_{GBT} \\ \boldsymbol{\zeta} \end{bmatrix} = \begin{bmatrix} \boldsymbol{F}_{SFE} \\ \boldsymbol{F}_{GBT} \\ \boldsymbol{0} \end{bmatrix}, \tag{29}$$

where $\boldsymbol{K}_{SFE}$ and $\boldsymbol{K}_{GBT}$ are the global stiffness matrices of the shell macro-element and GBT-based finite elements, respectively, and $\boldsymbol{F}_{SFE}$, $\boldsymbol{F}_{GBT}$ are the associated nodal force vectors. Although the system is symmetric, matrices $\boldsymbol{B}_{SFE}$ and $\boldsymbol{B}_{GBT}$ are generally neither symmetric nor square.

The system (29) can be simplified by eliminating the Lagrange multipliers and condensing the shell macro-element DOFs, leading to a system involving only the GBT DOFs. Besides leading to a great economy of DOFs, this procedure is particularly useful if a shell macro-element library is available in the code (i.e., the linear stiffness matrices of several types of member connections are already available) and/or the macro-elements appear at several locations in the model (which is typical in steel structures).

For the bifurcation problem, the same principles apply. Several numerical techniques for condensing DOFs are available (see, e.g., [25]), the simplest one consisting of setting the corresponding sub-matrices of $\boldsymbol{G}$ to zero, which is equivalent to the standard static condensation of massless DOFs in a lumped mass model, for the calculation of natural frequencies. However, since the examples presented in this paper do not involve many DOFs, no condensation of the shell DOFs was performed.

4. Numerical examples

4.1 Lipped channel cantilever with a tapered segment

The first example concerns a lipped channel cantilever beam with a tapered segment. Figure 4 (a) shows the beam geometry and material parameters. The height of the tapered part of the beam varies linearly for $0 \leq X \leq 0.25$ m, remaining constant thereafter.

The GBT cross-section discretisation employed is shown in Figure 4 (a). With this discretisation, 39 deformation modes are obtained. As mentioned before in Section 2.2, only the natural Vlasov (modes 1 to 6) and local-plate modes (modes 7 to 15) are included in the analyses (see Figure 4 (b)).

Three models are analysed: (i) a full shell model with 2220 elements, (ii) a less refined GBT-shell model, where only the tapered zone is discretised with a shell macro-element (550 shell elements + 10 GBT elements), and (iii) a refined GBT-shell model where the shell macro-element is extended 0.25 m into the uniform height zone (1100 shell elements + 5 GBT elements).

Figure 5 (a) displays the linear analysis results, namely the deformed configurations, the GBT mode amplitude diagrams and the displacements of points P1 and P2 identified in this figure (the differences with respect to the full shell model are also displayed).

Concerning the displacements of points P1 and P2, the results show that both GBT-shell solutions match very accurate the full shell model one (differences below 1%), a fact which is confirmed by the very good agreement between the deformed configurations displayed in the figure.

The mode amplitude diagrams make it possible to conclude that minor axis bending (mode 3) and symmetric distortion (mode 5) are the most important. In fact, the deformed configurations provided in the figure clearly corroborate this remark. Near the transition zone, for the less refined GBT-shell model, several local-plate modes also appear, even if their contributions are at least one order of magnitude below those of modes 3 and 5 (these participations are hardly noticeable in the diagram, near $x = 0$). On the other hand, the modal participation diagram of the refined GBT-shell model is essentially a truncated version of the less refined one. Consequently, the local-plate modes in the tapered-uniform transition zone no longer appear. This shows that, as pointed out in Section 3, extending the shell macro-element zone increases the dissipation of local deformation effects stemming from the transition and, furthermore, makes it possible to use less deformation modes in the GBT-based element (in this case, it is possible to discard the local-plate modes).

Next, a linear stability analysis of the cantilever is carried out to determine the first buckling load (the load profile consists of 2×1 kN point loads) and the corresponding buckling mode. Once more, the previous three models are considered (see Figure 5 (b)).

In this case, the mode amplitude diagrams show that the buckling modes are essentially distortional, although major axis bending also participates along the beam, and local-plate modes appear near the GBT-shell transition zone. The GBT-shell refined model leads to a bifurcation load nearly coincident to the full shell model. Once more, the benefits of extending the shell macro-element beyond the tapered-uniform transition zone are clear: accuracy increases and the participations of the local-plate modes become much smaller. It is worth remarking that the buckling loads obtained by the GBT-shell models are slightly lower than those provided by the full shell model as a consequence of the lack of complete compatibility along the GBT-shell interface. Nevertheless, the differences obtained are very small for the extended GBT-shell model (1.33%).

4.2 Lipped channel cantilever with two long holes

The second example consists of a lipped channel cantilever with the same material parameters and cross-section of the uniform segment of the previous example (see Figure 4 (a)), but having two long holes located exactly in the middle of each flange. The beam geometry is displayed in Figure 6. Concerning the loadings, the linear analysis is performed for a 1 kN lateral load (along $-Y$), applied at one of the flange-lip corners near the cantilever mid span, whereas for the bifurcation analysis the loading consists of a 1 kN load applied at the flange-web corner of the free-end section, along $-Z$.

Three models are considered: (i) a shell model without the holes, to assess their influence (1650 elements), (ii) a shell model with the holes (1590 elements) and (iii) a GBT-shell model where a shell macro-element is employed for the 0.55 m central segment of the beam (660 shell elements + 10 GBT elements). The linear and bifurcation analyses results are reported in Figure 7.

The linear analysis results are first examined. A comparison between the shell models depicted in Figure 7 (a) with and without holes shows that the latter yields a much stiffer response, providing a 73% lower lateral displacement of the point of load application. The GBT-shell model captures the shell model (with holes) deformed configuration very accurately, with a small difference (2%) in terms of the displacement of the point of load application. Furthermore, the modal participation diagrams provided in the figure make it possible to conclude that the zones without the holes undergo essentially major-axis bending (mode 2), torsion and symmetric (mode 5) plus anti-symmetric (mode 6) distortion. The con-

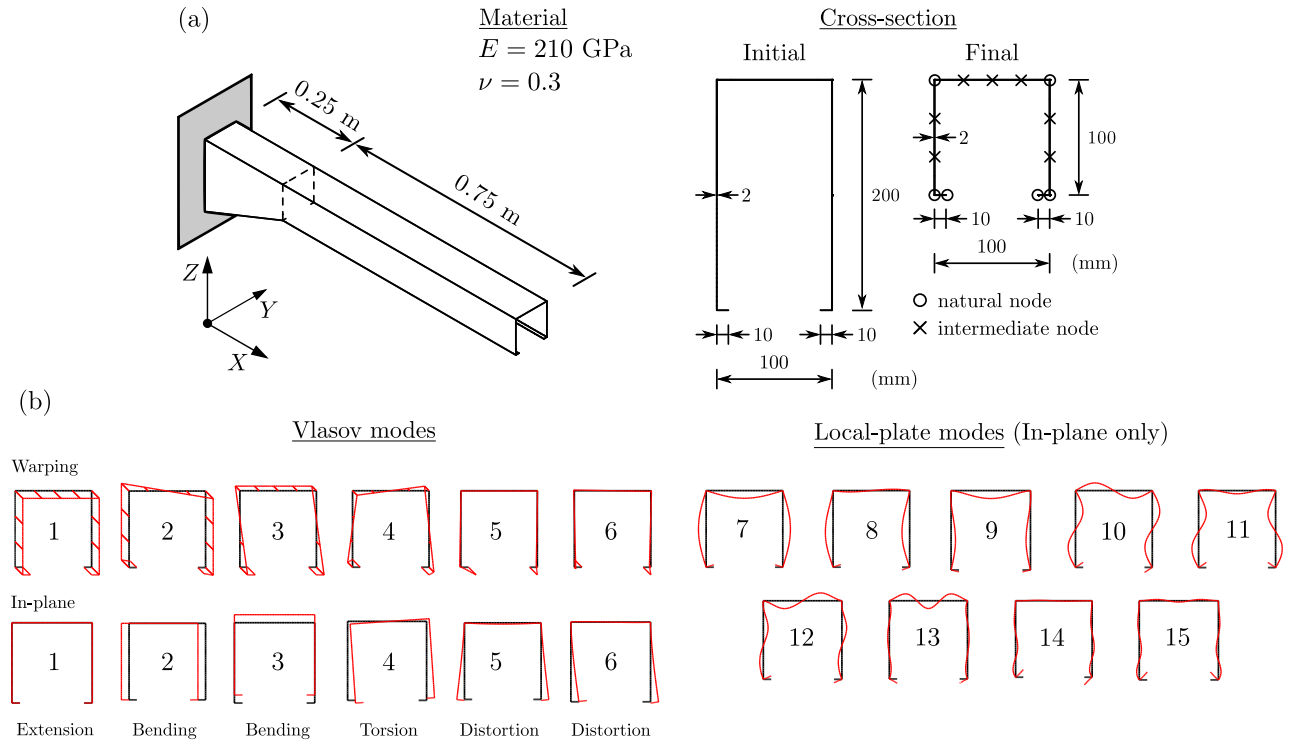

Figure 4: Lipped channel cantilever: (a) geometry and GBT cross-section discretisation, and (b) first 15 cross-section deformation modes.

tributions of local-plate modes are virtually null.

Consider now the bifurcation analysis results displayed in Figure 7 (b). The holes play again a very significant role, namely in the critical load parameter, which is more than 20% higher in their absence, and in the buckling mode shapes: (i) with holes, the mode is characterised by a pronounced distortion in the right hole zone, with a significant inward lateral displacement of the lip, whereas (ii) without holes, cross-section distortion mostly occurs near the support. The GBT-shell model captures the buckling mode quite accurately and provides a critical load which falls within 2% of the shell model one.

The modal participation diagrams concerning the buckling mode make it possible to conclude that both segments without holes essentially undergo distortion (modes 5 and 6) and that the free end zone also exhibits bending and some torsion.

4.3 L-shaped frame with a tapered joint

The third and last example consists of the L-shaped frame depicted in Figure 8 (a). The joint has a complex tapered geometry that influences significantly the frame structural behaviour. Consequently, the joint zone is discretised with a shell macro-element. Concerning the loadings, the linear analysis is carried out with an eccentric 10 kN vertical force, applied at the flange outstand of the free end, whereas for the bifurcation analysis the force is changed to a 1 kN load and moved to the top web-flange intersection. It is also worth noting that, in the bifurcation analysis, two lateral supports are provided at the free end cross-section, in order to obtain a buckling mode involving complex lateral-torsional-local displacements at the joint (otherwise the critical buckling mode essentially involves lateral-torsional buckling of the horizontal beam).

The GBT the cross-section discretisation shown in Figure 8 (a) is adopted, involving a single intermediate node in the web. The relevant deformation modes included in the GBT finite element are displayed in Figure 8 (b) and consist of only 4 natural Vlasov and 5 local-plate modes.

Figure 9 shows the results of the linear and bifurcation analyses. In both cases two models are compared: (i) a shell model (2801 elements) and (ii) a GBT-shell model (1151 shell elements + 10 GBT elements).

The linear analysis results show that, in spite of the complexity of the structure, the GBT-shell model yields a vertical displacement of the point of load application which is virtually identical to that provided by the shell model (0.17% difference). The GBT mode amplitude diagrams provided on the right of Figure 9 (a) show that the vertical member essentially undergoes in-plane and out-of-plane bending, whereas

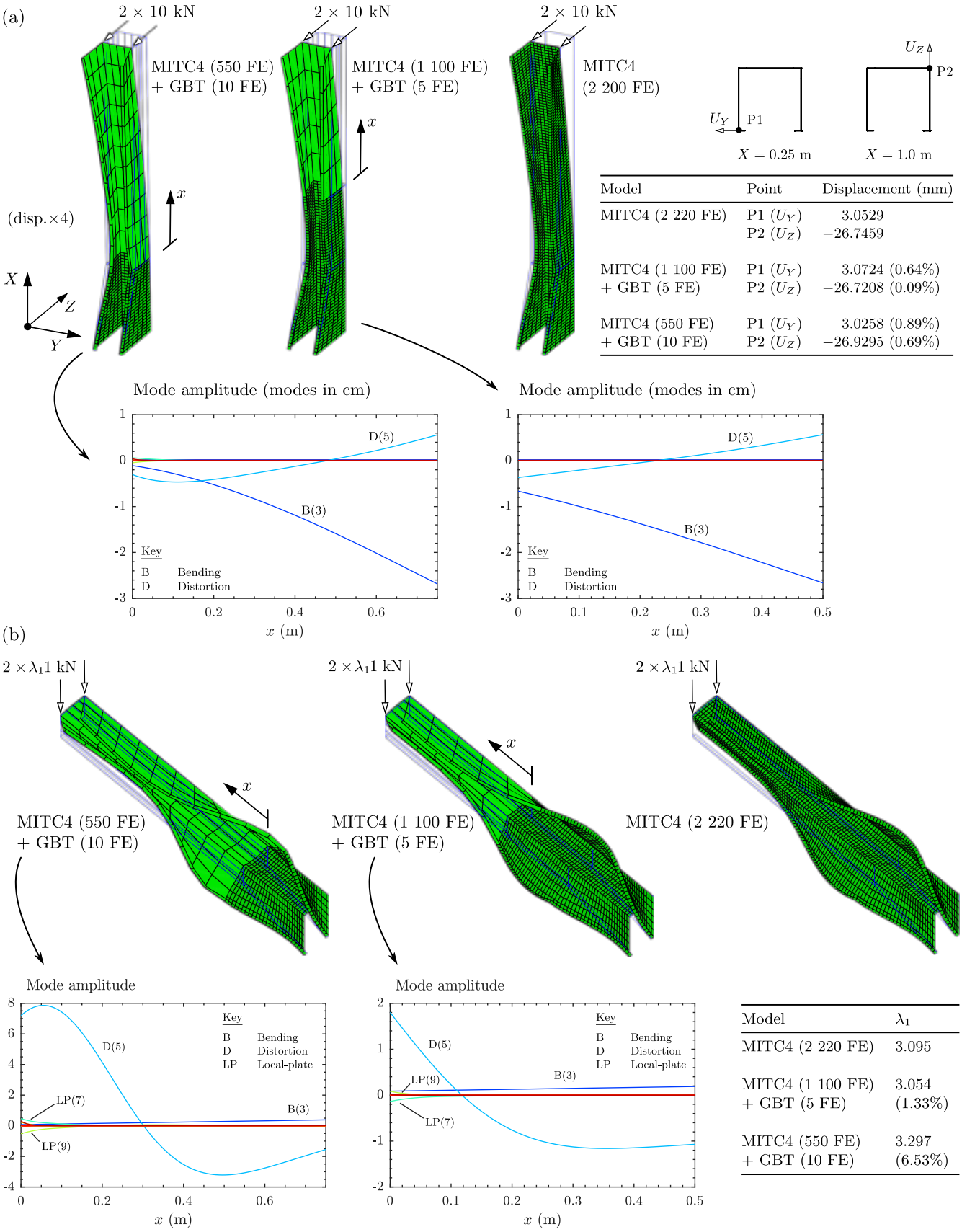

Model	Point	Displacement (mm)
MITC4 (2 220 FE)	P1 (U_Y)	3.0529
	P2 (U_Z)	−26.7459
MITC4 (1 100 FE) + GBT (5 FE)	P1 (U_Y)	3.0724 (0.64%)
	P2 (U_Z)	−26.7208 (0.09%)
MITC4 (550 FE) + GBT (10 FE)	P1 (U_Y)	3.0258 (0.89%)
	P2 (U_Z)	−26.9295 (0.69%)

Model	λ_1
MITC4 (2 220 FE)	3.095
MITC4 (1 100 FE) + GBT (5 FE)	3.054 (1.33%)
MITC4 (550 FE) + GBT (10 FE)	3.297 (6.53%)

Figure 5: Lipped channel cantilever: (a) linear analysis and (b) bifurcation analysis (first buckling load).

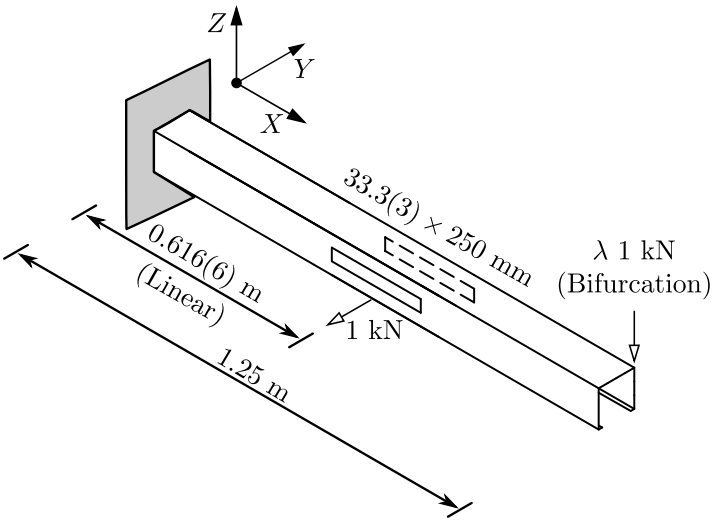

Figure 6: Lipped channel cantilever with two long holes.

the horizontal beam exhibits a more complex behaviour, involving mostly bending and torsion, but also local effects near the free end, due to the influence of the point load. Also note that, in the horizontal member, the axial extension mode has a constant participation, which indicates that, as expected, it undergoes a rigid-body horizontal displacement.

Concerning the bifurcation results shown in Figure 9 (b), it should be first noted that the critical buckling mode exhibits a very complex behaviour at the joint, which can only be adequately captured with shell elements. Nevertheless, the proposed GBT-shell approach yields excellent results, with a critical load difference of only 3.5%. The modal participation diagrams make it possible to conclude that the buckling behaviour of the prismatic members is almost purely global (i.e., the local-plate modes have almost null participations), thus confirming that the complex behaviour is restricted to the joint zone.

5. Concluding remarks

This paper presented an efficient approach to analyse thin-walled members with complex geometries and connections, combining standard shell and GBT-based finite elements. The GBT elements are used to model prismatic member segments, whereas the complex zones (discontinuities, holes, joints, etc.) are dealt with using shell elements, creating shell macro-elements. For this approach, two major advantages can be pointed out: (i) the number of deformation modes employed in the GBT elements can be reduced and (ii) the shell macro-elements can be condensed out of the global equilibrium equation system, leading to a very high DOF economy and ensuring fast computation times. The latter advantage is especially important if the complete structure involves many identical macro-elements.

For validation and illustrative purposes, three numerical examples were presented and discussed, concerning (i) a lipped channel cantilever with a tapered segment, (ii) a lipped channel cantilever with long flange holes and (iii) an L-shaped frame with a tapered joint. Linear and bifurcation (linear stability) analyses were carried out in all cases and the results obtained with the proposed approach were compared with full shell models. All the cases shown an excellent agreement.

As a final note, it is mentioned that the authors are currently extending this approach to other types of structural analyses.

6. Acknowledgments

The first author gratefully acknowledges the financial support of FCT (Fundação para a Ciência e a Tecnologia, Portugal), through the doctoral scholarship SFRH/BD/130515/2017.

References

[1] R. Schardt, “Eine Erweiterung der Technischen Biegetheorie zur Berechnung prismatischer Faltwerke”, *Stahlbau*, vol. 35, pp. 161–171, 1966, (German).

[2] R. Schardt, *Verallgemeinerte Technische Biegetheorie*. Berlin, Germany: Springer Verlag, 1989, (German).

[3] D. Camotim, C. Basaglia, R. Bebiano, R. Gonçalves, and N. Silvestre, “Latest developments in the GBT analysis of thin-walled steel structures”, in *Proc. Int. Coll. Stability and Ductility of Steel Struct.*, E. Batista, P. Vellasco, and L. Lima, Eds., Rio de Janeiro, Brazil, 2010, pp. 33–58.

[4] D. Camotim and C. Basaglia, “Buckling analysis of thin-walled steel structures using generalized beam theory (GBT): State-of-the-art report”, *Steel Construction*, vol. 6, no. 2, pp. 117–131, 2013.

[5] M. Nedelcu, “GBT formulation to analyse the behaviour of thin-walled members with variable cross-section”, *Thin-Walled Structures*, vol. 48, no. 8, pp. 629–638, 2010.

[6] M. Nedelcu, “GBT formulation to analyse the buckling behaviour of isotropic conical shells”, *Thin-Walled Structures*, vol. 49, no. 7, pp. 812–818, 2011.

[7] A.-A. Muresan, M. Nedelcu, and R. Gonçalves, “GBT-based FE formulation to analyse the buckling behaviour of isotropic conical shells with circular cross-section”, *Thin-Walled Structures*, vol. 134, pp. 84–101, 2019.

[8] J. Cai and C. D. Moen, “Elastic buckling analysis of thin-walled structural members with rectangular holes using generalized beam theory”, *Thin-Walled Structures*, vol. 107, pp. 274–286, 2016.

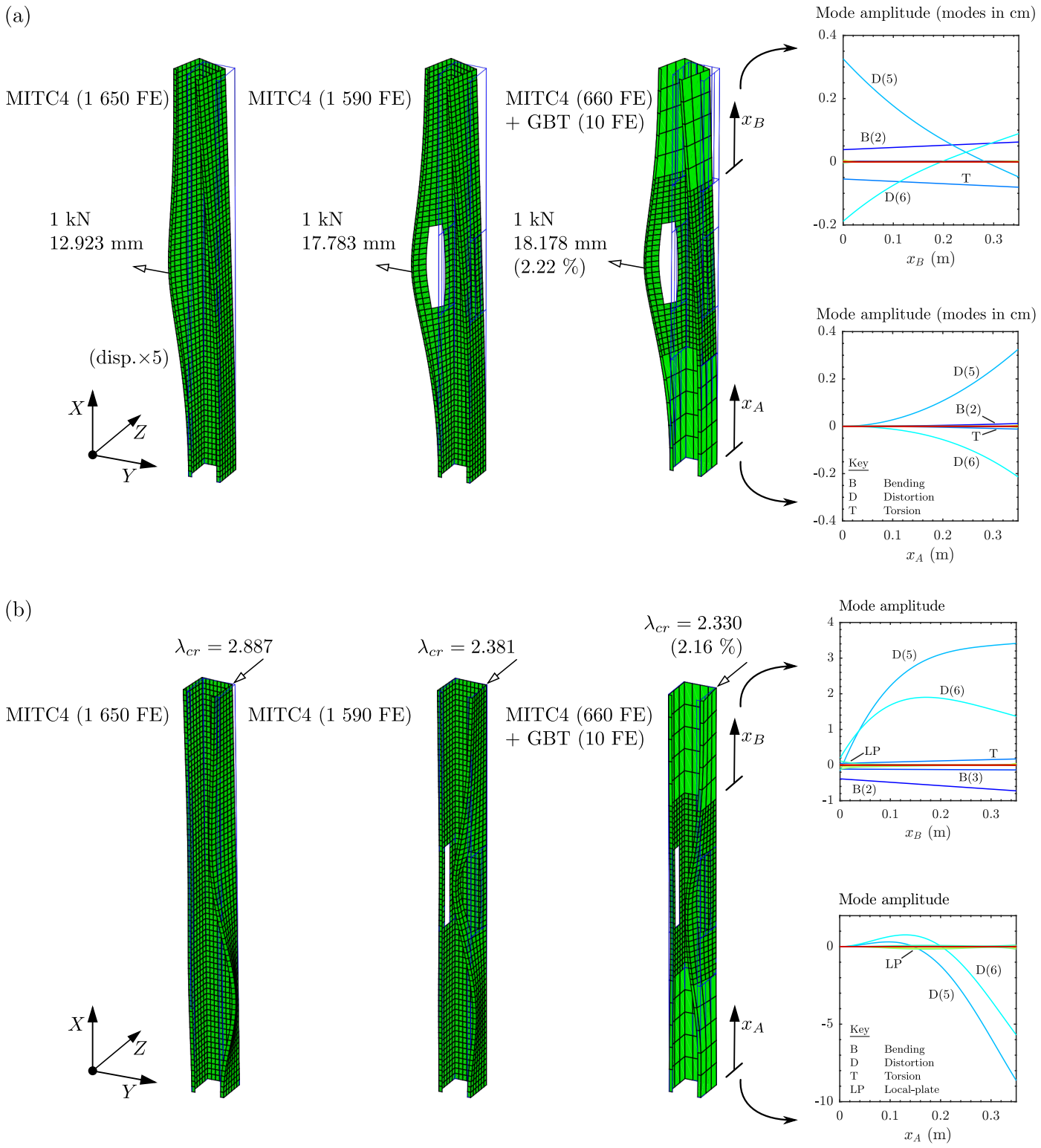

Figure 7: Lipped channel cantilever with two long holes: (a) linear analysis and (b) bifurcation analysis.

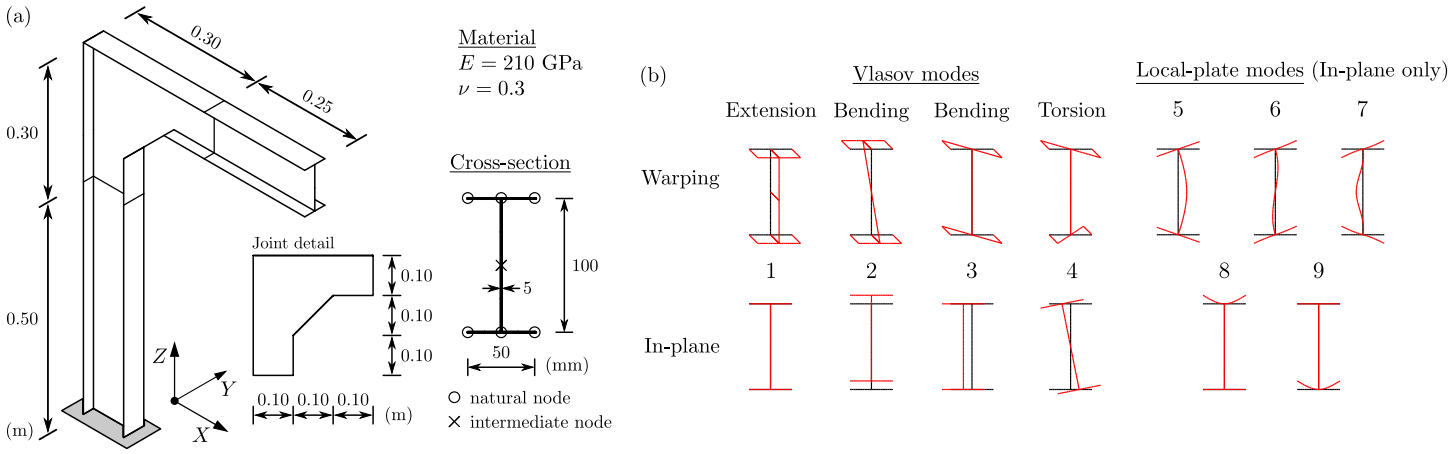

Figure 8: L-shaped frame with a tapered joint: (a) geometry and (b) GBT deformation modes.

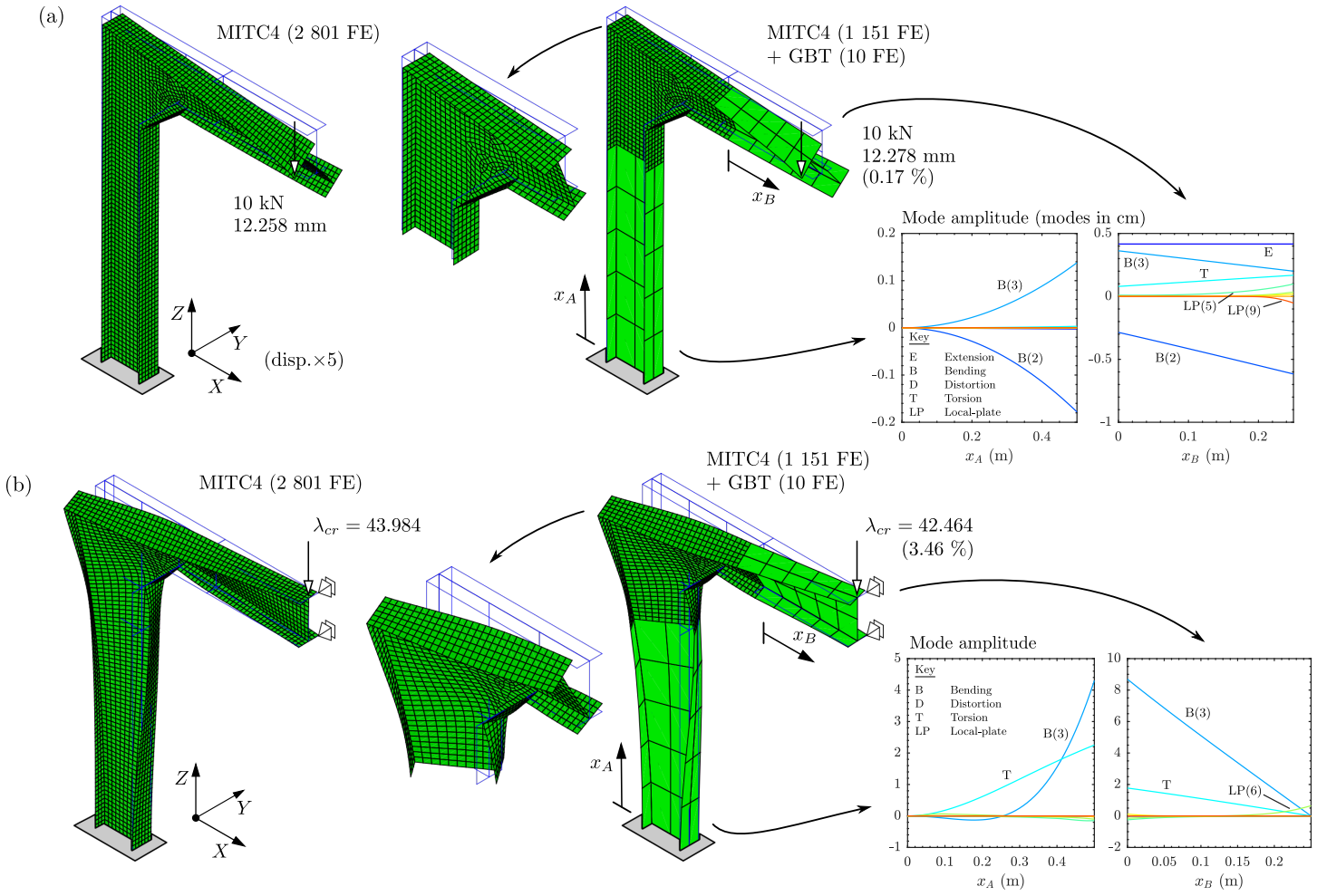

Figure 9: L-shaped frame with a tapered joint: (a) linear analysis and (b) bifurcation analysis.

[9] R. Gonçalves and D. Camotim, "Improving the efficiency of GBT displacement-based finite elements", *Thin-Walled Structures*, vol. 111, pp. 165–175, 2017.

[10] N. Peres, R. Gonçalves, and D. Camotim, "First-order generalised beam theory for curved thin-walled members with circular axis", *Thin-Walled Structures*, vol. 107, pp. 345–361, 2016.

[11] N. Peres, R. Gonçalves, and D. Camotim, "GBT-based cross-section deformation modes for curved thin-walled members with circular axis", *Thin-Walled Structures*, vol. 127, pp. 769–780, 2018.

[12] C. Basaglia, D. Camotim, and N. Silvestre, "Global buckling analysis of plane and space thin-walled frames in the context of GBT", *Thin-Walled Structures*, vol. 46, no. 1, pp. 79–101, 2008.

[13] C. Basaglia, D. Camotim, and N. Silvestre, "GBT-based local, distortional and global buckling analysis of thin-walled steel frames", *Thin-Walled Structures*, vol. 47, no. 11, pp. 1246–1264, 2009.

[14] D. Camotim, C. Basaglia, and N. Silvestre, "GBT buckling analysis of thin-walled steel frames: A state-of-the-art report", *Thin-Walled Structures*, vol. 48, pp. 726–743, Oct. 2010.

[15] C. Basaglia, D. Camotim, and N. Silvestre, "Post-buckling analysis of thin-walled steel frames using generalised beam theory (GBT)", *Thin-Walled Structures*, vol. 62, pp. 229–242, 2013.

[16] K. J. Bathe and E. N. Dvorkin, "A four-node plate bending element based on Mindlin/Reissner plate theory and a mixed interpolation", *International Journal for Numerical Methods in Engineering*, vol. 21, no. 2, pp. 367–383, 1985.

[17] K. J. Bathe, *Finite element procedures*, 1st ed. New Jersy, USA: Prentice-Hall, Inc., 1996.

[18] D. Manta, R. Gonçalves, and D. Camotim, "Combining shell and GBT-based finite elements: Linear and bifurcation analysis", *Thin-Walled Structures*, vol. 152, p. 106 665, 2020.

[19] R. Gonçalves and D. Camotim, "Geometrically non-linear generalised beam theory for elastoplastic thin-walled metal members", *Thin-Walled Structures*, vol. 51, pp. 121–129, 2012.

[20] R. Gonçalves, R. Bebiano, and D. Camotim, "On the shear deformation modes in the framework of Generalized Beam Theory", *Thin-Walled Structures*, vol. 84, pp. 325–334, 2014.

[21] R. Bebiano, R. Gonçalves, and D. Camotim, "A cross-section analysis procedure to rationalise and automate the performance of GBT-based structural analyses", *Thin-Walled Structures*, vol. 92, pp. 29–47, 2015.

[22] R. Bebiano, D. Camotim, and R. Gonçalves, "GBTUL 2.0 – a second-generation code for the GBT-based buckling and vibration analysis of thin-walled members", *Thin-Walled Structures*, vol. 124, pp. 235–257, 2018.

[23] R. Gonçalves, P. L. Grognec, and D. Camotim, "GBT-based semi-analytical solutions for the plastic bifurcation of thin-walled members", *International Journal of Solids and Structures*, vol. 47, no. 1, pp. 34–50, 2010.

[24] M. Ainsworth and B. Senior, "Aspects of an adaptive hp-finite element method: Adaptive strategy, conforming approximation and efficient solvers", *Computer Methods in Applied Mechanics and Engineering*, vol. 150, no. 1, pp. 65–87, 1997.

[25] T. Hitziger, W. Mackens, and H. Voss, "High performance computing", in, H. Power and C. Brebbia, Eds. London: Elsevier, 1995, ch. A condensation-projection method for generalized eigenvalue problems, pp. 239–282.